ACS APPLIED NANO MATERIALS

www.acsanm.org

Article

Nanocrystalline Hexagonal Boron Nitride Thin Films Deposited by Dynamic Glancing Angle Deposition for UV-Emitting Devices and Detectors

Saron R. S.de Mello, Felipe Cemin, Fernando G. Echeverrigaray, Mawin J. M. Jimenez, Vanessa Piroli, Fábio J. R. Costa, Carla D. Boeira, Leonardo M. Leidens, Antonio Riul Jr, Carlos A. Figueroa, Luiz F. Zagonel, Antonio R. Zanatta, and Fernando Alvarez*

Cite This: *ACS Appl. Nano Mater.* 2025, 8, 12380−12392

Read Online

ACCESS | Metrics & More | Article Recommendations | Supporting Information

ABSTRACT: This study investigates thin films of hexagonal boron nitride (*h*-BN), a promising material for the development of UV optoelectronic and wide-band gap semiconductor applications. A comprehensive analysis of the structural and optical properties of *h*-BN films deposited by radio frequency sputtering, using both stationary and Dynamic Glancing Angle Deposition (DGLAD) techniques, demonstrates that the film nanostructure can be effectively tailored by controlling key deposition parameters such as substrate bias, deposition plasma composition, and substrate oscillation. The introduction of hydrogen into the deposition atmosphere promotes the formation of *turbostratic* polycrystalline films with tunable crystallite sizes and significantly impacts the bonding environment, leading to a controlled shift of the optical band gap from ~3.7 to ~4.2 eV. Substrate oscillation modulates the angle of precursor impinging on the substrate, influencing the nano- and microstructure of the films and their optical properties. The physical characteristics introduced by the specific method of preparation of *h*-BH, such as morphological and topographical features, were characterized via SEM and AFM. At the same time, photoluminescence (PL) measurements revealed defect-related emission states, highlighting the influence of structural disorder on radiative transitions. Importantly, the DGLAD approach emerges as a useful strategy to engineer the structural and optical features of the *h*-BN films. The reported findings provide valuable insights into the correlation between growth dynamics, crystallographic disorder, and optoelectronic properties, reinforcing the potential of *h*-BN for integration into UV photodetectors, light-emitting devices, and other possible wide-bandgap electronic applications such as sensors.

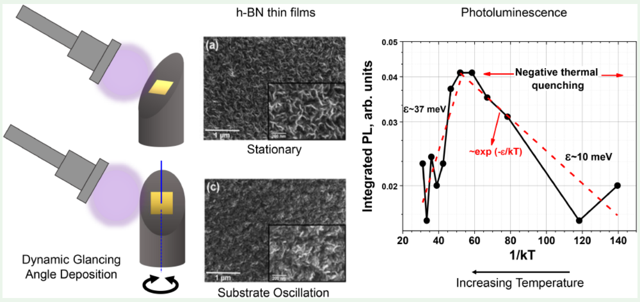

KEYWORDS: *h-BN, sputtering, thin films, photoluminescence, semiconductor*

1. INTRODUCTION

Hexagonal boron nitride (*h*-BN) is a layered material characterized by alternating nitrogen and boron atoms arranged in a hexagonal lattice, with atoms bonded by covalent bonds and multilayers linked by van der Waals (vdW) interaction forces, which contribute to its unique properties.[1] This material, when thinned down to a monolayer, has a relatively high band gap energy (~6 eV)[1], while staked-multilayer or bulk thin films present a band gap energy varying between ~4.5 eV[2] up to ~5 eV. Due to these properties, *h*-BN is proposed to be used in electronic and optical heterostructures such as UV-emitting devices and detectors.[3] As a versatile material, *h*-BN is often employed as an interface for charge fluctuation reduction, a passivation layer, a dielectric layer, and a tunnel barrier, and it is considered the most compatible interface to anchor graphene layers to substrates.[1,4,5] When doped, the material modifies its optical properties.[6,7] These modifications involve atomic rearrangements, generally at the grain boundaries, point defects such as atomic vacancies, as well as changes in the edge nanocrystals structure and the multilayer stacking building along the growth direction of the film,[8] all together impacting their optical, electrical, and magnetic properties.[6,7,9] Despite their advantages, the controlled synthesis of *h*-BN thin films with well-defined structural and optical properties remains a significant challenge. One of the primary difficulties lies in tailoring the crystalline and morphological properties of the films, which directly affects their optical band gap and emission characteristics. Moreover, the presence of structural disorder and defects

Received: May 2, 2025
Revised: May 19, 2025
Accepted: May 23, 2025
Published: June 3, 2025

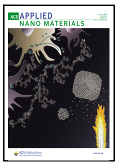

https://doi.org/10.1021/acsanm.5c02214

Table I. Typical Parameters for Deposited *h*-BN Films by the RF Magnetron Sputtering Technique.[a]

	φ = Flow (sccm)					
Samples	$[Ar_2]$ (±0.4)	$[N_2]$ (±1)	$[H_2]$	$[H_2\%] = \frac{[H_2]}{[Ar_2] + [N_2] + [H_2]}$	Bias (V) (±1)	P (s) (substrate oscillation period)
$S_{control}$	4.0	10	0	0	0	Stationary
S_1	4.0	10	0.40 ± 0.04	2.8 ± 0.5	0	Stationary
S_2	4.0	10	0.8 ± 0.1	5.4 ± 0.7	0	Stationary
S_3	4.0	10	0.40 ± 0.04	2.8 ± 0.5	−20	Stationary
S_4	4.0	10	0.40 ± 0.04	2.8 ± 0.5	−40	Stationary
S_5	4.0	10	0.40 ± 0.04	2.8 ± 0.5	−60	Stationary
S_6	4.0	10	0.40 ± 0.04	2.8 ± 0.5	−50	120
S_7	4.0	10	0.40 ± 0.04	2.8 ± 0.5	0	120

[a] The parameters maintained constant in all depositions are: RF power and frequency (P_{RF} = 75 W), pressure (p = 2.0 ± 0.2 Pa), substrate temperature (T = 400 ± 5 °C), and deposition time (t = 4 h)

often hinders the performance and reproducibility of potential devices based on *h*-BN. In this context, strategies that enable fine control over film nanostructure (such as dynamic deposition techniques and plasma composition engineering) open new opportunities for tuning the material's functional properties.

Plasma-based methods, including reactive magnetron sputtering and plasma-enhanced chemical vapor deposition, are used to produce *h*-BN thin films forming hexagon nanowalls growing fairly perpendicular to the substrate surface,[10−13] in a *turbostratic* structure. The nanowall formation results from the hydrogen addition in the gaseous mixture constituting the plasma during deposition. Therefore, the hydrogen role is 2-fold: occupying interstitial sites in the atomic boron nitride arrangement by breaking weaker bonds and inducing vertical columnar growth.[10,11] Moreover, due to the *turbostratic* nanocrystalline structure,[14] these films present band gap energy values of ∼4.5 eV. Furthermore, it has been shown that the physical and mechanical properties of thin films grown using physical vapor deposition techniques can be improved by combining these standard techniques with the DGLAD technique, allowing the formation of different nanostructures and unique anisotropic properties.[15,16]

Consequently, they have potential for application in optoelectronic devices for energy storage and heterostructure systems such as *h*-BN/graphene and *h*-BN/TiO_2[17,18] heterostructures. Merenkov et al. have shown that these films are very stable and have bactericidal properties by direct contact of the microorganism cell with the nanowalls, proving efficient cytotoxicity.[19,20]

In summary, this work presents a study of *turbostratic*-nanocrystalline *h*-BN films deposited using magnetron sputtering and the DGLAD technique. The latter technique was employed to explore the influence of the precursor's incidence angle, substrate biasing, and hydrogen on peculiar properties of the *h*-BN. This study explores the hitting variable angle of the precursors, which transfer momentum to the atoms forming the film, increasing their mobility, diffusion, and coalescence, contributing to controlling the material properties. Indeed, the dynamically changing angle of the precursors landing on the substrate due to the oscillation, combined with the role of hydrogen, biasing substrate, adds a set of parameters controlling the process, showing the viability of tailoring the structure of the films (nanowalls), crystallite size, optical gap, and luminescence properties.

Allied with the spectroscopic analysis of the plasma (during deposition), we present and discuss structural, vibrational, optical, morphological, and topographical characterizations, and compositional analysis of these films. Therefore, this study provides a systematic, comprehensive evaluation of the produced film's properties and correlation with their structure as a function of the deposition processes. Additionally, we evaluated the influence of deposition conditions on the optical photoluminescent emission. By temperature-dependent PL spectroscopy, we have discussed the probable mechanisms driving the observed emission characteristics, such as the negative quenching temperature.

2. EXPERIMENTAL SECTION

2.1. Thin Film Deposition. Equipped with a sputtering gun (ST20 AJA International), the deposition system operates with a radio frequency (RF) power supply (13.56 MHz, Lesker R301), a maximum 300 W generator, and a standard automatic impedance adaptation controller. A negative bias voltage is applied to the substrate by a DC power supply (JBM MP1503D). A low-voltage halogen lamp controlled by a standard proportional-integral-derivative (PID) heating system maintained the substrate temperature constant. The PID setup allows tuning the best matching of the proportional (adjusting the temperature band), integral (adjusting the proportional bandwidth), and derivative (to minimize overshoot or undershoot) to keep the temperature desired. A molecular turbopump (Edwards nEXT400) evacuated the reactor chamber. Mass flow controllers (MKS 600 Series) are employed to feed the reactor with the appropriate gaseous mixtures. The boron target purity is 99.95%, 2 in. diameter, and 0.25" thick. The reactor base pressure reaches (3.0 ± 0.3) × 10^{-4} Pa. All samples were cleaned before the deposition by an argon (99.995% purity) plasma at ∼1.1 × 102 Pa for 5 min employing a current-controlled pulsed power supply (4 kW-PlasmaLiits). The substrate is etched by applying a pulse of 50 μs (on) and 120 μs (off), −350 V amplitude, and 60 mA current for 10 min with the substrate properly masked.

The films were deposited (thickness of 670 ± 30 nm) on quartz and monocrystalline silicon (100) substrates (P type, B doped, resistivity 0.1−1.0 ohm·cm). Study-selected films were deposited by the DGLAD technique for comparison purposes by adopting a triangular function (T = 2 min oscillation period) motion of the substrate. Further details about this technique can be found elsewhere.[16] Table I displays the deposition conditions used on this set of samples, with

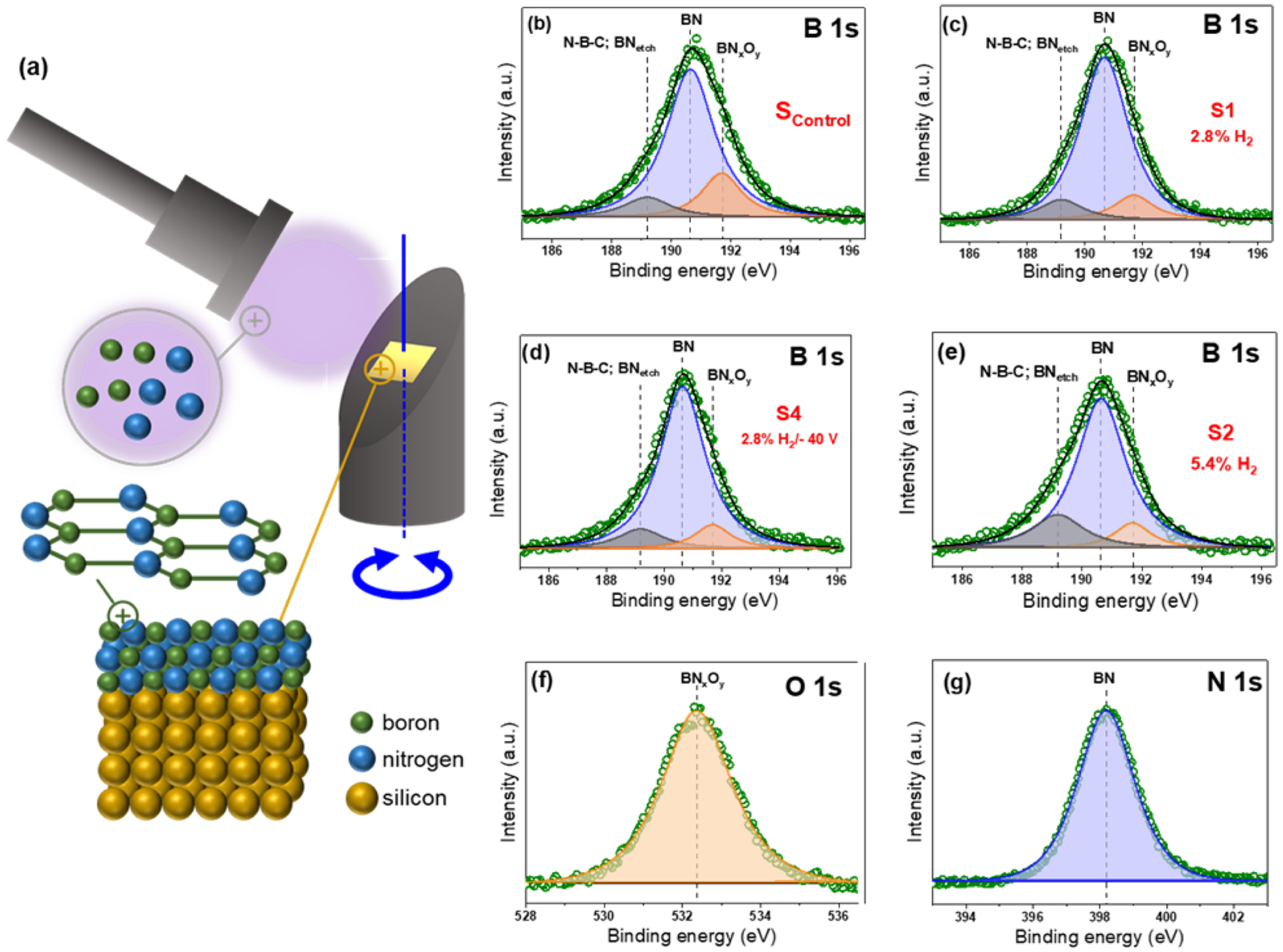

Figure 1. (a) Sketch of the *h*-BN film deposition system by plasma-assisted DGLAD and schematic atomic structure. Photoemitted electron intensity vs binding energies spectra as obtained by XPS. Boron-related photoelectrons (1s orbital) of different films: (b) $S_{control}$, (c) S_1, (d) S_2, and (e) S_4. Photoelectron core levels associated with (f) oxygen (1s) and (g) nitrogen (1s) for samples grown in the presence of H_2 during deposition (except for $S_{Control}$).

variations to the gas flow (φ), bias, and period (T) oscillation used for each deposition.

2.2. Sample Characterizations. *2.2.1. X-ray Photoelectron Spectroscopy.* X-ray photoelectron spectroscopy (XPS) was employed for analysis of the relative atomic composition. The chemical states of the elements that constitute the samples and relative film composition were obtained by XPS (Thermo Alpha 110 Hemispherical Analyzer operated in constant pass energy mode at 20 eV, Al Kα radiation, nonmonochromatic). The total system resolution is ~1.15 eV (~0.85 eV radiation line width plus ~0.3 eV analyzer resolution). To determine the analyzer's work function, the binding energy associated with the 3d$_{5/2}$ electrons of silver (Ag, 368.2 ± 0.1 eV) was used for binding energy calibration.[21] The analyzer pressure is maintained at $<1.10^{-9}$ Pa during the measurements. The samples were cleaned (~9 min) by argon ions (Ar+) plasma by a broad ion beam-assisted cell attached to the XPS system.[21] The ion beam system consists of a 1 in. diameter Kaufman cell used with a 400 eV voltage and a nominal current of 20 mA. Due to beam divergence, the ion beam diameter on the substrate (located at ~20 cm from the gun) presents a diameter of ~12 cm, i.e., a current density of 0.18 mA/cm^2 covering the sample and part of the substrate stainless steel holder. By employing the Thermo Scientific Advantage software, a combined Gaussian and Lorentzian function was used to deconvolute areas. The spectral band associated with the different photoemitted electrons permits the estimation of the atomic compositional percentages of the studied films.[22] Then, the relative atomic concentrations were calculated by applying the appropriate sensitive correction factors of each component given by the Wagner et al. method.[23]

2.2.2. X-ray Diffraction. X-ray diffraction (XRD) was employed to evaluate the bulk crystalline structures of the films identified by Shimadzu equipment (XRD-6000) operating in Bragg−Brentano θ-2θ configuration with a Cu Kα (1.5406 Å) monochromatic radiation source produced at 40 kV and 30 mA. Crystallite size film was estimated by applying the single-line analysis method of Keijser et.al.[24] The *Grazing* incidence X-ray diffraction technique (GIXRD) was employed to investigate the surface crystalline structure. The analysis angle range was from 20 to 70° with a 0.01°/s step, 1° grazing incidence, and 5 s time/step. The equipment had a Rigaku Ultima IV X-ray unit with a Cu Kα (1.5406 Å) monochromatic radiation source produced at 40 kV and 30 mA.

2.2.3. Raman Scattering Spectroscopy and Fourier Transform Infrared Spectroscopy. To investigate the vibrational properties of the samples, Raman scattering spectroscopy and Fourier−transform infrared spectroscopy (FTIR) were employed. The Raman spectra (Renishaw RM2000, backscattering geometry) were acquired in the 50−2500 cm^{-1} range by exciting the samples at 632.8 nm (HeNe laser, 5 μW power). The spectra were collected with an objective lens of 50x probing of a 1 μm^2 area. The FTIR measurements (PerkinElmer Spectrum, 32 scans, 4 cm^{-1} resolution) were made in the 400−4000 cm^{-1} range with an attenuated total reflection (ATR) module. All experiments were conducted under room conditions.

2.2.4. Field Emission Scanning Electron Microscopy. Field emission scanning electron microscopy (FE-SEM) was used to study the morphological characteristics from images (Oxford Instruments, Tescan Mira), 12 kV, working distance between 4.9 − 6.0 mm, and a secondary electron detector (SE). Top and cross-sectional images were also made using a dual-beam electron microscope, scanning electron microscope with a focused ion beam (FIB, Thermo Fisher Scientific, Helios NanoLab 660), voltage between 2 and 5 eV, working distance to 1.9−2.2 mm, and secondary and backscattered electrons (BSE) detectors.

2.2.5. Ultraviolet−Visible. Ultraviolet−visible (UV−vis) spectroscopy was used to evaluate the reflectance and optical transmittance spectra in the range of 215−1050 nm wavelength (~5.7−1.2 eV energy range) by a spectrometer with transparent UV−visible optical fibers (Ocean Optics HR 4000). The analyzed area and spectral resolution remained ~3 mm^2 (spot diameter of 2 mm) and <10 nm, respectively.

Additional information was gathered using photoluminescence (PL) measurements at various temperatures by exciting films with 488.0 nm photons in the ~500−750 nm wavelength range. Later, we shall discuss the relatively large line width of the PL bands stemming from topological disorder.[25]

3. RESULTS AND DISCUSSION

3.1. Chemical Environment and Composition. To provide a comprehensive overview of the system, Figure 1a presents a schematic illustration highlighting the structure and fabrication route of the thin films. The sketch shows the plasma-assisted deposition of *h*-BN films using the dynamic glancing angle deposition (DGLAD) technique alongside a simplified atomic-scale representation of the resulting nanostructure. Considering this system, Figure 1b−g displays the XPS spectra of the *h*-BN films after cleaning by argon ions, highlighting clear contributions due to the boron-, nitrogen-, and adventitious residual oxygen-related core levels, along with their proposed deconvolution for samples growing in the presence of H_2 during deposition. Figure 1b−e shows the boron binding energy spectra (B 1s orbital) of selected samples: $S_{control}$ (Figure 1b), S_1 (Figure 1c), S_2 (Figure 1d), and S_4 (Figure 1 e). XPS analysis was not carried out on samples previously obtained by DGLAD since, based on previous studies,[15,26] it does not affect the films' atomic composition. Furthermore, all the samples deposited using substrate bias (i.e., S_3, S_4, and S_5) exhibited similar spectra.

All the photoelectrons associated with the B 1s orbital in boron−nitrogen bonds exhibit a main band at ~190.6 eV.[27−31] The band located at ~191.7 eV refers to the nonstoichiometric compound BN_xO_y commonly observed in the 191.6−192.1 eV region of the spectra.[29,31] The contribution obtained by the proposed deconvolution at ~189.2 eV represents the presence of nonstoichiometric, nitrogen-deficient boron nitride, i.e., (BN_{1-x}), which is reported in the 188.5−189.3 eV region.[29] The origin of the nitrogen deficiency stems from the preferential sputtering effect during the cleaning process. Finally, within the experimental conditions, no bands associated with atomic boron (~187.3 eV energy) and boron oxide (B_2O_3) (~193.5 eV energy) were detected.[40,42,43,45]

Figure 1f shows the oxygen binding energy associated with electrons in the O 1s orbital samples grown in the presence of H_2 during deposition (except for $S_{Control}$). There is a single band at ~532.3 eV referring to BN_xO_y compounds in the 531.9−532.4 eV binding energy range.[30] There are no bands related to B_2O_3 compounds (binding energy expected at ~533.2 eV), which validates what was previously found for the B 1s spectra.[27,28] Figure 1g represents the spectral band associated with samples grown in the presence of H_2 during deposition (except for $S_{Control}$), with electron binding energies in the N 1s orbital (~398.2 eV, energy range reported 398−398.7 eV) found in BN compounds. There are no representative bands that can be associated with nitrogen bonded to oxygen (NO) at the expected energy ~402 eV. The FWHM values for all spectra were 2.1 ± 0.2 eV. This suggests the existence of disorder and/or small microcrystalline size distribution.[21] It is also important to consider that the presence of oxygen forming BN_xO_y, C−N, and C−B compounds prevents the stoichiometric formation of *h*-BN. This experimental result is due to the affinity of oxygen, hydrogen, and carbon elements present in the plasma during deposition, as revealed by XPS. It is worth noting that oxygen atmospheric contamination can be hosted in porous nanostructures present in the *h*-BN nanowalls and that ex-situ XPS analysis has intrinsic limitations in this context. However, the comparative analysis between samples remains valid and informative under the consistent treatment conditions applied.

These results are in accord with the structural properties of the *turbostratic* samples, as obtained from the photoluminescence and Raman experiments, in which the broad spectra indicate the presence of disorder. Moreover, this consideration will be revisited with regard to X-ray diffractogram analysis. The emission of chemical species observed by XPS spectra agree with the emission spectroscopy obtained during the deposition of the films (Figure S1). Regarding the estimated films' relative atomic composition after cleaning the surfaces of the samples as a function of the hydrogen gas mixture during the deposition, they are shown in the Figure S2a. From this plot, two pieces of information can be obtained. First, boron (~45%) and nitrogen (~35%) relative atomic concentrations, within the experimental errors, remained constant in the studied films.

Second, the oxygen presence as a contaminant is visible, reducing from ~12% to ~5% after hydrogen feeding in the chamber during plasma depositions. This suggests that hydrogen atoms promote etching and/or passivation of reactive sites, as well as oxygen atoms' preferential removal by chemical affinity in the H_2O formation and elimination via pumping.

InFigure S2b, the results of an analysis of the concentrations relative to the BN band analysis based on deconvolution of the spectra represented by Figure 1a−d are shown above. This estimated bond percentage decreased after the hydrogen presence in the plasma, ranging from ~18% to ~9% (~50% reduction of oxygen atomic concentration). The sample

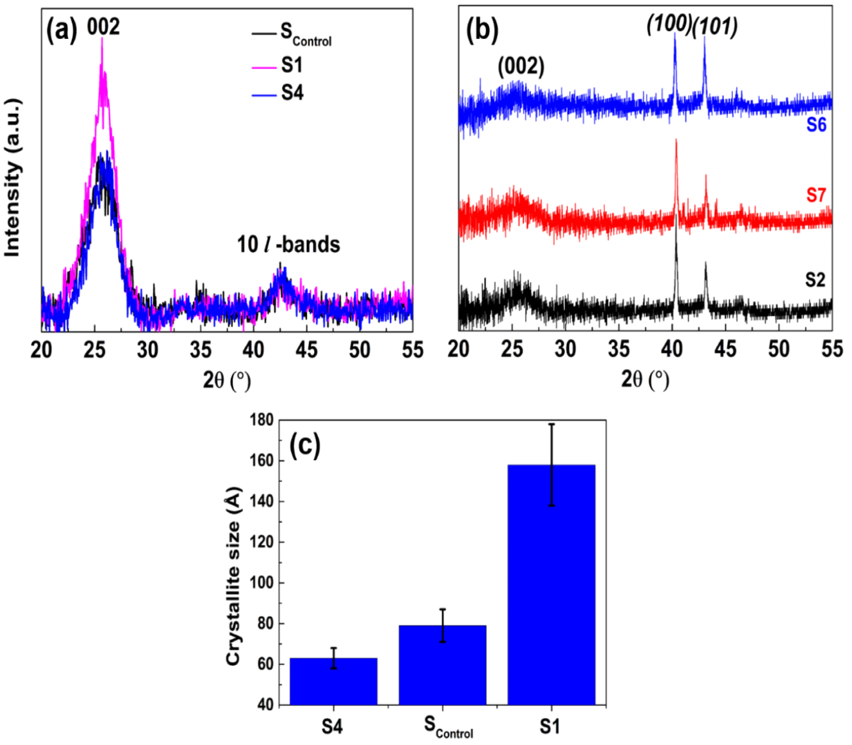

Figure 2. (a) X-ray diffractograms of $S_{Control}$, S_1, and S_4. (b) X-ray diffractograms with grazing incidence of samples S_2, S_6, and S_7. (c) Calculated crystallite size for the main diffraction band in the XRD diffractograms associated with the (002) planes.

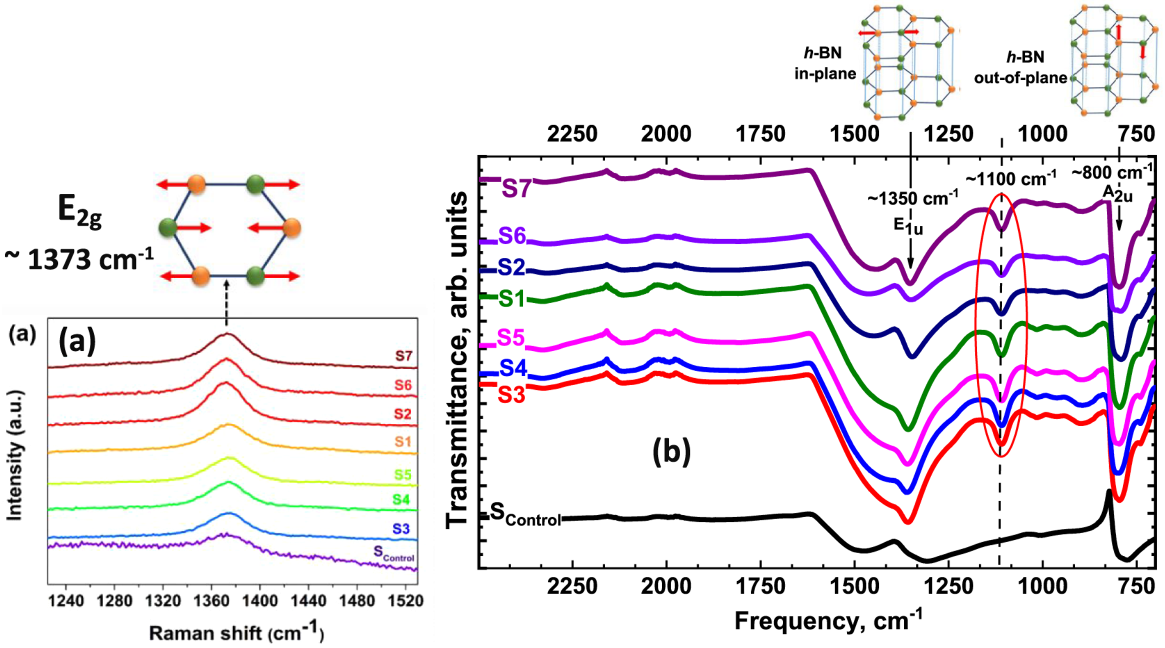

Figure 3. (a) Raman spectra of all samples, highlighting the band at ~1373 cm^{-1} that refers to the E_{2g} vibrational mode. (b) FTIR-ATR spectra of all samples. The bands at ~1350 cm^{-1} and ~800 cm^{-1} refer to the E_{1u} and A_{2u} vibrational modes, respectively.

deposited applying substrate bias (S_4) (not present in Figure S2) shows results similar to those of sample S_1. So, biasing the substrate did not affect the composition.

3.2. Crystallographic Properties. Figure 2a presents the X-ray diffractograms of the $S_{control}$, S_1, and S_4 samples. The general features of diffractograms are similar. The relatively more intense diffraction band around 26° corresponds to (002) planes (a fingerprint of the BN hexagonal structure), and the wider bands indicate the nanocrystalline material.[32,33] Moreover, the relatively less intense and broader band at ~42.5° corresponds to the superposition of diffractions at ~41.6° and ~43.9° associated planes (100) and (101). This has already been observed in *h*-BN nanocrystals due to (100) and (101) stacking fault planes, characteristic of a *turbostratic* structure.[14] Figure 2b shows the grazing incident angle diffractograms obtained from the S_2 sample and the samples deposited by the DGLAD technique, with (S_6) and without biased substrate (S_7). These results are qualitatively similar to those observed by regular XRD, except that the underneath diffractions at (100) and (101) are well resolved.[34]

As remarked previously, crystallites with *turbostratic* structure exhibit the *h*-BN local hexagonal-like structure, i.e., without long-range order between layers, similar to an amorphous network.[32,35,36] Furthermore, the diffraction band referring to the (002) plane shifts to smaller diffraction angles compared to the reported angle ~26.7°, corresponding to *turbostratic*, i.e., disorder.[35,37,38] As discussed before, the wide bands observed in the XPS spectra were ascribed to inhomogeneous disorder, a consistent hypothesis with the XRD results, as well as, we shall see later on, in the photoluminescence results.

Calculated crystallite size values are presented in Figure 2c. As commented above, they were estimated by applying the single-line analysis method of Keijser et.al.,[24] considering the main peak of the XRD diffractograms associated with the (002). The peaks were fitted by a Voigt function, assuming that the Lorentzian and Gaussian components of the line profile are due to both the crystallite size and strain, respectively. Hydrogen, added to the gaseous mixture during the depositions, resulted in a crystallite size increase relative to the S_{control} sample. This is expected since hydrogen is saturating dangling bonds and defects, allowing the growth of crystallites and increasing the order of the material. As confirmed by XPS results, hydrogen is prompting *h*-BN formation by removing residual contaminant oxygen. On the other hand, sample bias increases the ion bombardment, which might prevent the crystallite size from increasing due to the constant sputtering by argon ion (Ar^+) during the film's growth.[39]

3.3. Vibrational Characterization of the Samples.

The samples' structural properties were studied also by vibrational spectroscopies such as Raman and Fourier-transform infrared (FTIR). These spectra are presented in Figure 3a,b, respectively. Crystalline *h*-BN belongs to the D^4_{6h} space group, and the symmetry transformations (at the center of the Brillouin zone) involving their optical phonons are given by $2E_{2g} + 2B_{1g} + A_{2u} + E_{1u}$. As a result, the E_{2g} modes are Raman active, the A_{2u} and E_{1u} are FTIR active, and the B_{1g} modes are optically inactive.[40,41]

The lowest frequency mode (~50 cm^{-1}) occurred when all planes slide against each other, while the boron and nitrogen atoms' movement against each other in the plane characterizes the highest frequency mode at ~1366 cm^{-1} (Figure 3a).[40−42] The Raman highest frequency mode is located at ~1373 cm^{-1}, corresponding to the sp^2 type bond elongation vibration between boron and nitrogen atoms in the hexagon plane (Figure 3a).[37,42] Considering the Raman signal of monocrystalline *h*-BN (~1366 cm $^{-1}$), the upper-shifting and relative line-broadening present in Figure 3a are indicative of a decrease in crystallite size. For polycrystalline *h*-BN, the E_{2g} vibrational mode characteristic line occurs between 1367 and 1374 cm^{-1}[40,41]. The sample deposited with a higher hydrogen content in the gaseous mixture (S_2) and the samples obtained by the DGLAD technique (S_6 and S_7) showed a ~2 cm^{-1} decrease in wavenumber values, closer to the reference (1366 cm^{-1}) value. In addition, compared to S_{control} (~40 cm^{-1}) and other samples (~38 cm^{-1}), samples (S_2, S_6, and S_7) exhibit smaller FWHM values (~36 cm^{-1}). The "lower-FWHM−higher-crystallite" size relationship indicates defect reduction.[40,43,44] Thus, the higher hydrogen content in the gaseous mixture favors *h*-BN crystal growth, which agrees with the X-ray diffractogram results. More information about Raman spectroscopy is presented in Figures S8 and S9.

FTIR spectra of all samples are presented in Figure 3b. There are two main bands associated with *h*-BN vibrational modes located at ~800 cm^{-1} and ~1350 cm^{-1}. The first one corresponds to the out-of-plane vibration mode named *R* or A_{2u}, where boron and nitrogen atoms move into or out of the hexagon plane (Figure 4b). The second one refers to an in-plane elongation and/or stretching in the hexagon plane (in-plane), it is labeled the L mode or E_{1u}, referring to the longitudinal vibration of the atoms (Figure 4b).[45] As noted in Figure 3b, S_{control} presents a subtle band compared with the other samples studied.

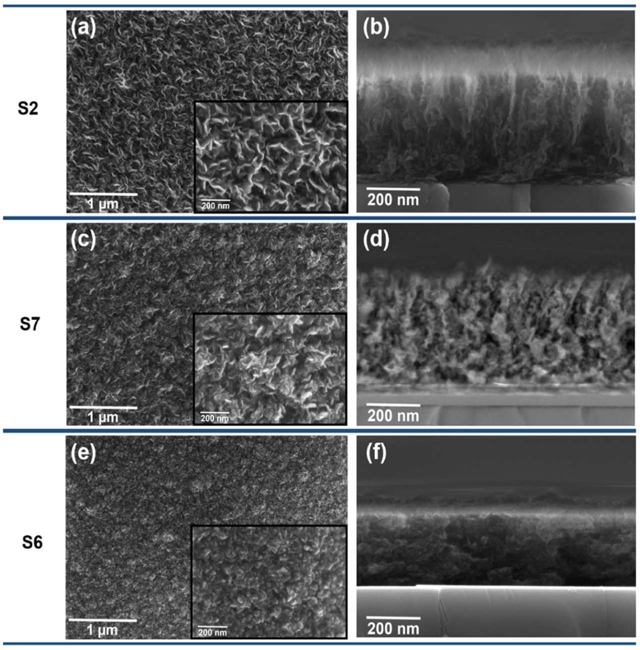

Figure 4. FIB-SEM images for the samples obtained with ~5.4% H_2 in stationary mode (S_2, columnar vertical growth) and the samples deposited by the DGLAD technique (S_6 and S_7, columnar zigzag growth). (a), (c), and (e) are top-view images. Scale bars in the bottom left corner are 1 μm. Zoom images have 200 nm scale bars. (b), (d), and (f) are cross-section images with 200 nm scale bars.

The band at ~1100 cm^{-1}, present in all sample spectra, except for the S_{control}, according to the literature, refers to boron, oxygen, and hydrogen bond (B−O−H), indicating that the presence of hydrogen in the gaseous mixture during the deposition results in important modifications in the structure of the film.[8,46] However, assigning this vibration to (B−O−H) is challenged by the fact that bulk BN shows a mode around this region of the spectra.[47,48]

3.4. Microstructure of the Films.

Figure 4a presents the top-view SEM image of the S_2 sample. The verified morphology of "twisted small wires" has been reported in the literature as nanowalls of hexagonal structures preferentially growing perpendicular to the substrate surface.[10,11,20,49] The morphological growth of this formation is evidenced in the SEM cross-sectional image, where columnar growth is apparent (Figure 4b).

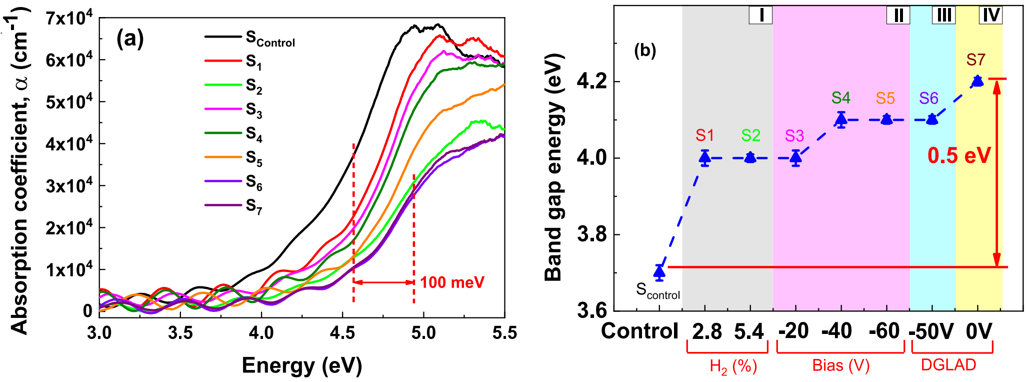

Figure 5. (a) Calculated absorption coefficient $\alpha(\text{cm}^{-1})$ as a function of phonon energy. The wavy-like pattern at low energies is due to interference effects at the film−substrate interface; (b) band gap energy values are calculated using the method described by Zanatta.[50] Dashed lines are guides for the eyes.

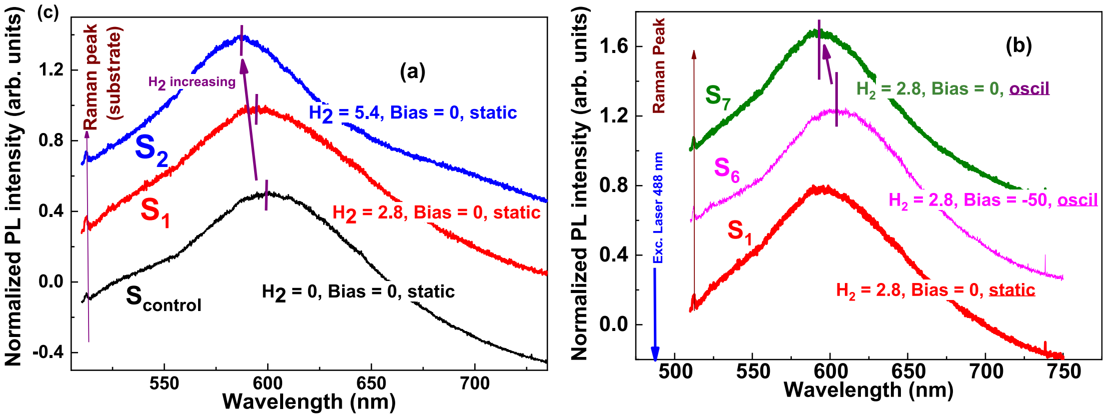

Figure 6. (a), (b) Room-temperature photoluminescence (PL) spectra of *h*-BN samples deposited by DGLAD sputtering under different conditions. In panel (a), the only deposition parameter that varied was the hydrogen concentration. In panel (b), the optical gap shifting is due to the DC bias applied to the substrate during the growth of the films, maintaining the hydrogen constant. The peak contributions at 512.3 nm originate from the c-Si substrate (2TO phonon). The spectra were normalized and vertically shifted for comparison purposes.

The top and cross-section SEM images of the sample obtained using the DGLAD technique and ~2.8% H_2 (S_7) are shown in Figure 4d, respectively, according to which the "twisted profile" and substrate perpendicular growth are observed. However, compared to Figure 4b, this sample seems to have a more disordered profile. This may be associated with the incident angle of the precursor species. Previous studies have shown that it is possible to obtain wavy columnar growth by the DGLAD technique.[26] Finally, Figure 4f show the top and cross-section images of the sample deposited by the DGLAD technique, ~2.8% H_2 and −50 V substrate biasing (S_6). In this case, compared to Figure 4c, the top-view image has a "granular" profile, and the cross-section shows a more compacted film than those observed in Figure 4d. The bias use favors denser film formation since the Ar^+ ion bombardment breaks weak bonds, resulting in a more compact film without nanowall formation. Figure S5 shows SEM top-view images of samples S_{control}, S_1, S_3, S_4, and S_5. Their morphology indicates greater crystallinity character in all samples compared to the control sample, as confirmed in the enlarged images.

3.5. Optical Characterization of the Films' Properties.

3.5.1. Band Gap Calculation. Supporting Information presents both the transmittance and reflectance spectra of the samples studied. Due to the *turbostratic*/nanocrystalline characteristic structure of the studied *h*-BN films, their optical band gap values were calculated by fitting a sigmoid (Boltzmann) function to the corresponding optical absorption spectra.[50]

The optical absorption edges span from ~3.7 eV (lower limit through the control sample (S_{Control})) to ~4.2 eV (upper limit with the sample S_6 deposited with 2.8% hydrogen content by the DGLAD technique). The effect of the deposition conditions on the absorption coefficient can be seen in Figure 5b.

The optical absorption spectra of Figure 6a present a systematic shift toward higher energy values, i.e., opening the band gap, starting with the S_{control} sample and ending with the DGLAD samples. The energy variation at the inflection point of these spectra has an overall 100 meV increment. Several factors modify the electronic structure of a material, affecting the optical band gap. It includes chemical composition and disorder, the presence of impurities or defects, lattice tensions, changes in grain boundaries, and distance between planes, influencing interatomic distances.[5−8,51−53] Figure 6b, Region I, shows that the band gap energy increases (~0.3 eV) with hydrogen addition to the gaseous mixture. As discussed previously, hydrogen insertion results in a decrease in the (nonintentional) oxygen content. The presence of oxygen, as well as carbon, induces intragap state formation where radiative electronic transitions are possible, as discussed later on in the photoluminescence results.[54] Another possible effect

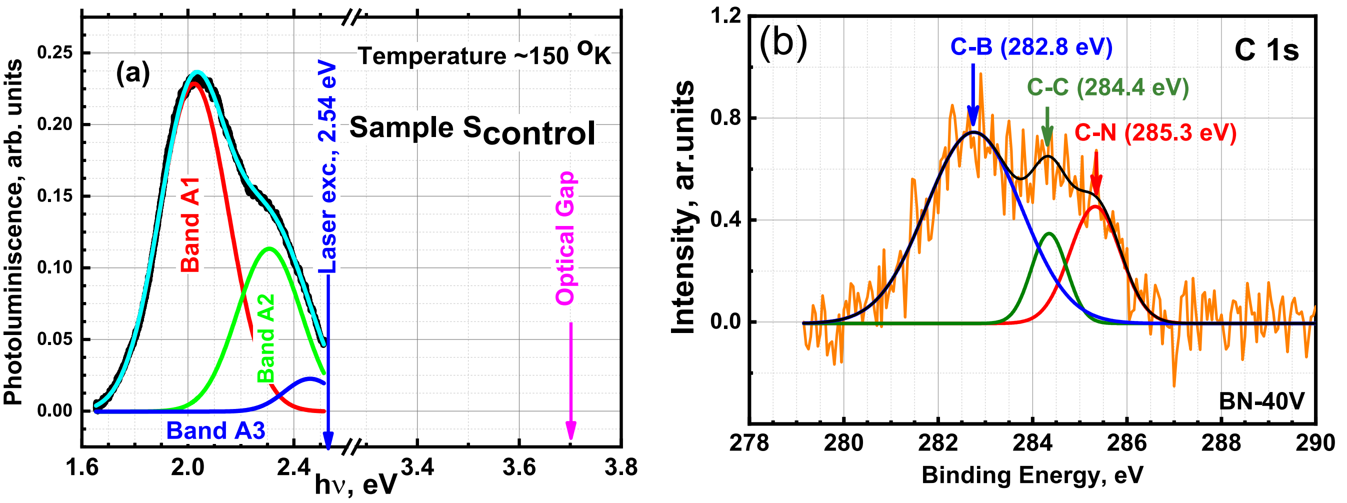

Figure 7. (a) PL spectra of the control sample ($S_{control}$) properly transformed to intensity versus energy, $E = h\nu$. This curve was taken as an example and deconvoluted into three components, as the shape of the emission of the samples suggests, as well as reported in the literature in *h*-BN carbon doped material:[54] (b) XPS of asample containing carbon stemming from the residual chamber's pressure.

caused by hydrogen is due to its insertion into the material structure, i.e., B−O−H bonds, as suggested by FTIR, controlling the states inside the gap, and modulating the band gap.[54,55] However, as commented above (Section 3), this vibration mode is close to the phonon associated with C-BN, and it could be an overlap of both the B−O−H and TO phonons of c-BN.

The substrate biasing resulted in a small band gap energy variation (~0.1 eV). This may be related to possible lattice strain that is generated by the bias applied in the substrate during the deposition.[53,56] Finally, the larger band gap value (~4.2 eV) is reached with the sample obtained by the DGLAD technique and 2.8% hydrogen in the gas mixture (S_7). This result indicates that there is a direct relationship between the incidence angle of the precursor species with the material structure changes, reaching a total band gap energy increase of ~0.5 eV.

3.5.2. Photoluminescence Properties. The PL spectra are complementary to UV−vis spectroscopy results, contributing to understanding the influence of the evolution and characteristics of the band gap of the material and its dependence on deposition conditions. The films were excited with a 488 nm laser wavelength, and in all cases, a distinct emission at ~512.3 nm is attributed to a Raman peak originating from 2TO phonons due to the c-Si substrate. Figure 7a shows the room-temperature PL spectra of the *h*-BN samples deposited under different conditions.

In Figure 6, the only deposition parameter varied was the hydrogen concentration ($H_2\% = 0$, 2.8, and 5.4), which caused the PL maximum to shift to a lower wavelength, compatible with an increasing optical gap observed in Figure 7b.

In Figure 7b, the optical gap shifting to a lower wavelength is due to the DC bias applied to the substrate while maintaining invariant H_2 during the growth of the films, which is also compatible with the small change of the optical gap (Figure 7b). The Raman and FTIR results previously discussed regarding the broadened spectra bands (FWHM) are consistent with the enlargement of the PL line shape.

To gain insight into the properties of the material, studies on the influence of the temperature on PL emission were conducted. It is noted that the shapes of the PL's spectra of all the studied samples are similar; i.e., three broader fixtures are present (see Supporting Information). Considering this observation, we proceeded to discuss just one of the sample representatives for the analysis of the experimental results of PL as a function of temperature.

Figure 7a shows the PL spectra of the control sample, $S_{control}$, measured at the temperature of 150 K, properly transformed to intensity vs energy[1], i.e., PL intensity versus $E = h\nu$. The deconvolution shows a good fit considering the contribution of a minimum of three components, as shown in Figure 7a. The variety of PL emission bands found in the literature is a result of the diverse microstructures, stoichiometry, and impurities involved in the phenomenon, justifying applying "Occam's Razor" to minimize the number of components.[57]

Therefore, the deconvolution procedure was satisfactory with three bands for all of the samples studied (see Figure S7 and Table S1). The bands A1 and A2, located at ~2.00 eV (~620 nm) and 2.32 eV (~535 nm) in Figure 9, are in reasonable agreement with the article of Wang et al.,[58] though they are prepared by different methods.

Although there are abundant articles discussing the photoluminescence of *h*-BN prepared by different techniques other than sputtering, preventing a comparison with the results of the present paper.[3,19,53,59], 86,[60] An exception is Prakash et al.,[61] who reported luminescence emission in BCN films deposited by dual target sputtering using B4C (DC gun) and BN (RF gun) targets. These researchers found two sharp peaks at ~597 and ~600 nm, near those reported in this paper, though sharper. Moreover, as we shall discuss below, this author also reported the interesting phenomenon of negative temperature quenching (NTQ), also found in our samples, suggesting similar structural characteristics of the material.

Figure 7b represents the *ex situ* XPS of a corresponding $S_{control}$ sample showing the presence of carbon stemming from the residual chambe's pressure and atmospheric contamination. This result is similar to that of all the samples. The sample was previously cleaned by an ion beam bombardment, as explained in section 2, to guarantee the elimination of carbon deposited outside of the deposition reactor stemming from atmospheric contamination. The band associated with electrons in orbitals C 1s was deconvoluted into three

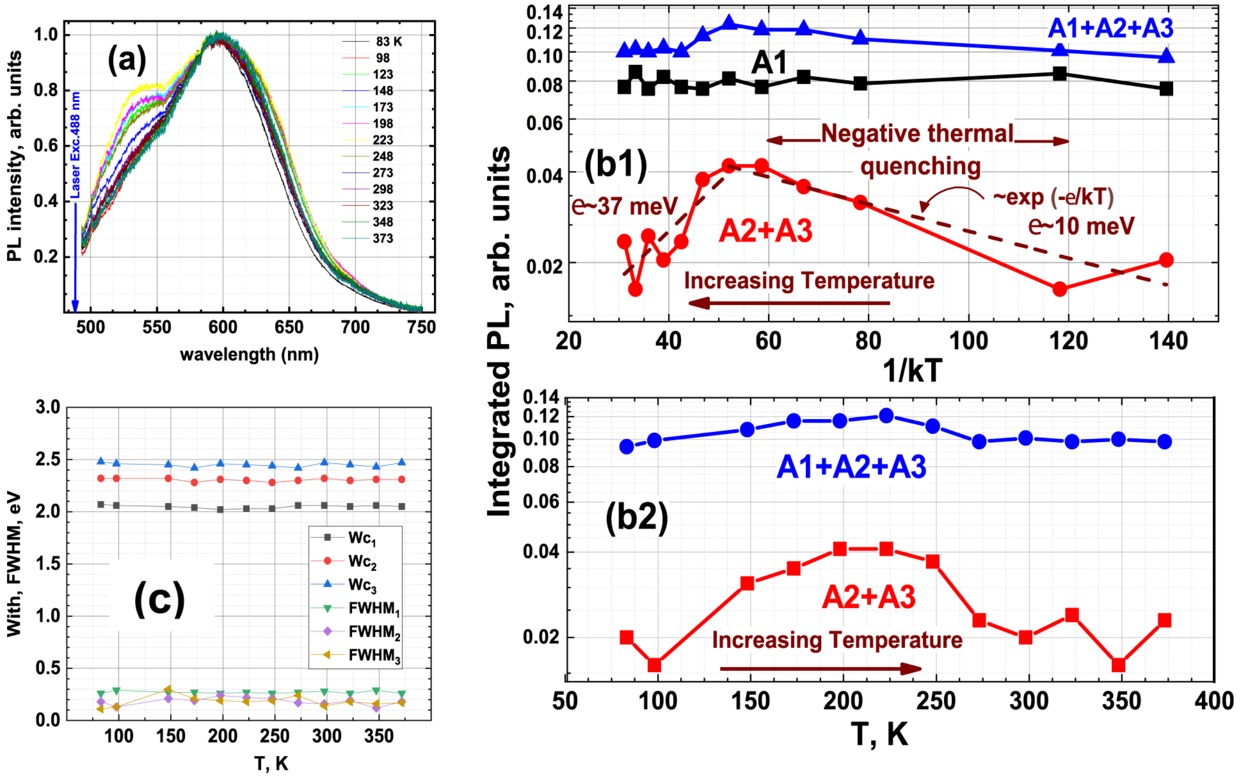

Figure 8. (a) PL experimental normalized integrated emission of the bands labeled (A1, A2, and A3) in Figure 8(a) corresponding to sample S_{control}; (b1) integrated emissions (A1 + A2 + A3), A1, and (A2 + A3), as a function of kT^{-1}. Note the unusual "negative thermal quenching" effect.[65] (b2) (A1 + A2 + A3) and (A2 + A3) as a function of T; and (c) FWHM$_i$ corresponding to full-width half-maximum and Wc$_i$ the maximum position of the peaks i = 1, 2, and 3 of the S_{control} as a function of T.

components, such as C−B, C−C, and C−N bonds.[62] From the experimental data, the carbon incorporated in the material is estimated to be ∼2−3 at%. As previously noted, XPS and FTIR (Figure 4b) showed oxygen contaminants in the samples studied (Section 2), an element considered to be involved in the emission photoluminescence. Figure 9 displays information related to the PL emission of sample S_{control} as a function of temperature.

Subplot (a) represents the normalized emission, where a prominent shoulder at ∼525 nm is evident. The broad PL emission is linked to radiative transitions associated with states near the top of the valence band of *h*-BN coatings doped with carbon and oxygen atoms.[54,63] The samples studied contain both elements, as shown in Figures 4 and 9. As commented in Section 3, Figure 4b shows a band at ∼1100 cm^{-1}, which is associated with a possible overlapping vibration mode due to B−O−H and c-BN structures.

However, it is important to note that oxygen is present in the material, as proven by XPS analysis (Figure 1), an element necessary together with carbon in the luminescence emission.

The *turbostratic* structure of *h*-BN is, to some extent, disordered, causing the enlargement of the PL bands (Figure 6) and also the absorption coefficient (Figure 5). Besides the disorder of the broad PL spectra, the electron−phonon interaction can contribute to the emission width.[25,64]

The deconvolution of individual curves from Figure 8a, following the procedure described in Figure 9a, allowed us to identify the bands A1, A2, and A3 in the space of energy $h\nu$ (eV) of the temperature dependence of this sample (Supporting Information). The first conclusion that we draw is that the main band A1, located at ∼2.02 eV, does not present any characteristic features. Indeed, within the experimental error, A1 is approximately constant as a function of 1/kT, as shown by the black square dots in (b1).

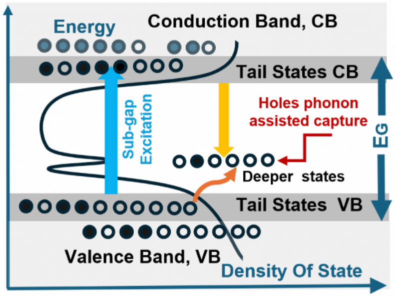

Figure 9. Energy band in the *h*-BN *turbostratic* studied material shows a density of states with some disorder, as suggested by the absorption coefficient (Figure 7) with an Urbach tail, as found in amorphous materials. The Deeper States indicated in the figure can capture hole due to phonon-assisted jumps causing the negative thermal quenching (NTQ) observed in Figure 9.

On the other hand, the sum of the A2 and A3 bands (red dots) shows the interesting features of negative thermal quenching (NTQ). It is interesting, as commented above, that NTQ was also reported by Prakash et al.,[61] a material also prepared by sputtering. In a recent review paper, Yan[65] discusses a broad bibliography on the NTQ subject and the debate about the physical explanation of the phenomenon. Several materials doped with rare earth, transition metals, Bi, and other elements presenting NTQ are discussed in the cited paper. Reports of *h*-BN photoluminescence generally show a normal quenching effect with temperature, i.e., decreasing intensity on increasing temperature.[60] Regarding PL in the *h*-BN material, Okashiro et al. reported NTQ in *h*-BN under anti-Stokes (AS) studies. These researchers excited the material with a 637 nm (∼1.95 eV) laser, obtaining maximum peak emission at ∼616 nm (2,01 eV), i.e., anti-Stokes PL emission.[66] However, normal Stokes PL in the same samples was observed; i.e., with 532 nm excitation (∼2.3 eV), the PL emission occurs at ∼610 nm (2.03 eV), and a normal quenching on temperature is obtained (Stokes emission). Differently, our study shows that a regular PL Stokes emission presents a region of NTQ effect, i.e., under subgap excitation, the PL intensity of the A1 + A2 band augments on increasing temperature up to ∼200 K. Further increasing temperature quenches the emission (Figure 9b1,b2). The observation of NTQ effects under subgap excitation was also related and modeled by Wang et al. in Si-doped GaN.[67] These authors assumed that hole acceptor states located near the valence band are thermally populated for holes with increasing temperature (i.e., phonon-assisted capture), enhancing the electron radiative recombination, i.e., increasing photoluminescence with increasing temperature, as is expected in the NTQ phenomenon. A heuristic qualitative model for the NTQ effect, motivated by the one discussed by Wangand coworkers, follows.[67] Figure 9 represents a proposed band scheme and density of states (DOS). This DOS is suggested by the absorption coefficient (Figure 9), where there is a wider absorption edge. Indeed, the *h*-BN *turbostratic* material owns nanocrystallites and, to some extent, disorder, giving rise to a wider absorption edge, as it occurs in hydrogenated amorphous silicon (a-Si:H). In Figure 7, the absorption edge presents three different regimes: (a) between 4.0 and 5.0 eV, the absorption coefficient increases slowly; (b) between 4.5 and 5.0 eV, the growing of the absorption is steepest, called Urbach tail; and (c) above 5.0 eV, the absorption coefficient tendency is to saturate.[68]

The decreasing slope of the Urbach tail in the *turbostratic h*-BN on deposition parameters is a fingerprint of increasing disorder (Figure 9), i.e., the origin of the tail states sketched in Figure 9. In fact, the absorption coefficient in disordered materials is basically a profile of the convolution of the top of the valence band and the bottom of the conduction band, i.e., basically, the tails of the DOS, since the conservation of the momentum $\underline{\mathbf{k}}$ in the electronic transition is not a requirement.[68]

Weng et al. reported that states associated with C and O bonds are located near the top of the valence band, as schematically indicated in Figure 9.[54] These states near the Urbach tail can be populated through phonon-assisted hole capture and subsequent radiative transitions (orange arrow), causing the NTQ observed in Figure 9. As commented above, the sub-bandgap PL emissions in *h*-BN are associated with point defects due to the intrusion of carbon (3−5 at%) and oxygen (∼5%) impurities present in the studied samples, as evidenced in Figure 8b. Moreover, the XPS spectra (section 2) and the FTIR spectral results[69,70] confirm the existence of these impurities. The precise structural nature of these defects remains a subject of ongoing debate, leaving room for the possibility that alternative defects are responsible for the observed emission. However, given the complexity of the growth process and the available information, attributing the observed emissions to any specific type of defect is beyond the current scope of this work.

4. CONCLUSIONS

This work demonstrates a successful deposition of *turbostratic*/nanocrystalline *h*-BN nanowalls via reactive magnetron sputtering using the dynamic glancing angle deposition (DGLAD) technique. Real-time optical emission spectroscopy confirmed the presence of boron and nitrogen species in the plasma, along with carbon and oxygen as contaminants. XPS analysis indicated that hydrogen incorporation in the plasma significantly reduces oxygen content in the films, from ∼12% to ∼5%, likely by the formation of volatile compounds, favoring B−N bond formation.

Structural characterization by XRD and Raman spectroscopy confirmed the *turbostratic*/nanocrystalline nature of the films. The presence of hydrogen increased the crystallite size by a factor of ∼25, while substrate bias induced its size reduction, highlighting the opposing roles of hydrogen and ion bombardment. SEM imaging showed vertically aligned nanowalls in static substrates and zigzag morphologies in oscillating ones. These structural variations are governed by the interplay between the hydrogen content, substrate bias, and DGLAD dynamics, which modulate the incidence of precursors impinging on the substrate.

Photoluminescence (PL) measurements showed broad emission bands consistent with some extent of structural disorder, as is expected in *turbostratic h*-BN. Remarkably, an anomalous NTQ effect was observed in Stokes PL: the emission intensity increased with temperature up to ∼200 K before conventional thermal quenching occurred. This behavior, typically absent in Stokes emission but previously reported in anti-Stokes PL of *h*-BN, suggests a thermally activated phonon-assisted recombination mechanism. More insight into the origin of this effect remains an open question, with potential implications for thermally light-emitting applications.

Finally, the precise control of the structural and optical properties of *h*-BN films is essential for several applications ranging from (simple) dielectric layers to microoptoelectronic devices, and the present work is expected to contribute to further advances in the field.

■ ASSOCIATED CONTENT

Supporting Information

The Supporting Information is available free of charge at https://pubs.acs.org/doi/10.1021/acsanm.5c02214.

Presents both the transmittance and reflectance spectra of the samples studied (MP4)

A file containing plasma optical emission spectroscopy − Figure S1; elements' bonding by XPS − Figure S2 ; topographical maps by AFM − Figure S3 ; roughness parameters − Figure S4 ; top view SEM microscopy − Figure S5 ; UV−Vis spectra − Figure S6 ; PL spectra − Figure S7 ; fitting parameters of the PL spectra − Table S1; Raman spectra − Figure S8 ; crystallite size − Figure S9 ; and FTIR analysis − Figure S10 (PDF)

■ AUTHOR INFORMATION

Corresponding Author

Fernando Alvarez − *Instituto de Física "Gleb Wataghin" (IFGW), Universidade Estadual de Campinas (UNICAMP), Campinas, São Paulo 13083-970, Brazil;* orcid.org/0000-0002-9393-1298; Email: alvarez@ifi.unicamp.br

Authors

Saron R. S.de Mello − *Instituto de Física "Gleb Wataghin" (IFGW), Universidade Estadual de Campinas (UNICAMP), Campinas, São Paulo 13083-970, Brazil;* Present Address: S.R.S.deM., current address: Univ. Grenoble Alpes, CNRS, CEA/LETI-Minatec, Grenoble INP, Institute of Engineering and Management University Grenoble Alpes, LTM, Grenoble, F-38054, France. F.G.E

Felipe Cemin − *Instituto de Física "Gleb Wataghin" (IFGW), Universidade Estadual de Campinas (UNICAMP), Campinas, São Paulo 13083-970, Brazil;* orcid.org/0000-0002-8971-2113

Fernando G. Echeverrigaray − *Instituto de Física "Gleb Wataghin" (IFGW), Universidade Estadual de Campinas (UNICAMP), Campinas, São Paulo 13083-970, Brazil;* Present Address: F.M.A.R.N., Univ. D.F.J.C., Bogotá D.C, Colombia.

Mawin J. M. Jimenez − *Instituto de Física "Gleb Wataghin" (IFGW), Universidade Estadual de Campinas (UNICAMP), Campinas, São Paulo 13083-970, Brazil;* Present Address: CTI R. Archer, Campinas-SP, Brazil. M.J.M.J.

Vanessa Piroli − *Programa de Pós-Graduação em Engenharia e Ciência dos Materiais (PPGMAT), Universidade de Caxias do Sul (UCS), Caxias do Sul 95070-560, Brazil*

Fábio J. R. Costa − *Instituto de Física "Gleb Wataghin" (IFGW), Universidade Estadual de Campinas (UNICAMP), Campinas, São Paulo 13083-970, Brazil*

Carla D. Boeira − *Instituto de Física "Gleb Wataghin" (IFGW), Universidade Estadual de Campinas (UNICAMP), Campinas, São Paulo 13083-970, Brazil*

Leonardo M. Leidens − *Instituto de Física "Gleb Wataghin" (IFGW), Universidade Estadual de Campinas (UNICAMP), Campinas, São Paulo 13083-970, Brazil;* orcid.org/0000-0003-4552-1013

Antonio Riul Jr − *Instituto de Física "Gleb Wataghin" (IFGW), Universidade Estadual de Campinas (UNICAMP), Campinas, São Paulo 13083-970, Brazil*

Carlos A. Figueroa − *Programa de Pós-Graduação em Engenharia e Ciência dos Materiais (PPGMAT), Universidade de Caxias do Sul (UCS), Caxias do Sul 95070-560, Brazil;* orcid.org/0000-0002-9473-1626

Luiz F. Zagonel − *Instituto de Física "Gleb Wataghin" (IFGW), Universidade Estadual de Campinas (UNICAMP), Campinas, São Paulo 13083-970, Brazil;* orcid.org/0000-0002-4043-0318

Antonio R. Zanatta − *Instituto de Física de São Carlos (IFSC), Universidade de São Paulo (USP), São Carlos, São Paulo 13560-590, Brazil*

Complete contact information is available at:
https://pubs.acs.org/10.1021/acsanm.5c02214

Notes

The authors declare no competing financial interest.

■ ACKNOWLEDGMENTS

This study was financed, in part, by the São Paulo Research Foundation (FAPESP), grant 2019/18460-4. C.D.B. grant # 2022/08216-1 L.M.L. grant # 2023/07552-0. F.A., A.R.Jr, C.A.F., A.R.Z., and L.F.Z. are CNPq Fellows. This paper is part of the requirements of the master's degree dissertation of S.R.S.deM. (CAPES fellow − process 88887.473650/2020-00).

■ ADDITIONAL NOTE

[1] The total integrated PL radiation intensity must be constant in the λ (nm) as well in the hν (eV) space, i.e., $\int(I(\lambda)\mathrm{d}\lambda = \int I[(\lambda(h\nu)].\ J.\ \mathrm{d}(h\nu)$, where J is the Jacobian of the transformation λ (nm) to hν (eV). Then, as λ =hc/hv, $\mathrm{d}\lambda = \frac{\mathrm{hc}}{(\mathrm{hv})^2}\mathrm{d}(\mathrm{h}\nu)$, $J = \frac{\mathrm{hc}}{(\mathrm{hv})^2} = \frac{1240(\mathrm{nm{\cdot}eV})}{(\mathrm{hv})^2(\mathrm{eV})^2}$

■ REFERENCES

(1) Caldwell, J. D.; Aharonovich, I.; Cassabois, G.; Edgar, J. H.; Gil, B.; Basov, D. N. Photonics with Hexagonal Boron Nitride. *Nat. Rev. Mater.* **2019**, *4*, 552−567.

(2) Yamada, H.; Inotsume, S.; Kumagai, N.; Yamada, T.; Shimizu, M. Comparative Study of Boron Precursors for Chemical Vapor-Phase Deposition-Grown Hexagonal Boron Nitride Thin Films. *Phys. Status Solidi.* **2021**, *218* (3), 2000241.

(3) Song, S.-B.; Yoon, S.; Kim, S. Y.; Yang, S.; Seo, S.-Y.; Cha, S.; Jeong, H.-W.; Watanabe, K.; Taniguchi, T.; Lee, G.-H.; Kim, J. S.; Jo, M.-H.; Kim, J. Deep-Ultraviolet Electroluminescence and Photocurrent Generation in Graphene/HBN/Graphene Heterostructures. *Nat. Commun.* **2021**, *12* (1), 7134.

(4) Kim, K. K.; Lee, H. S.; Lee, Y. H. Synthesis of Hexagonal Boron Nitride Heterostructures for 2D van Der Waals Electronics. *Chem. Soc. Rev.* **2018**, *47*, 6342.

(5) Geng, D.; Yang, H. Y. Recent Advances in Growth of Novel 2D Materials: Beyond Graphene and Transition Metal Dichalcogenides. *Adv. Mater.* **2018**, *30*, 1800865.

(6) Ba, K.; Jiang, W.; Cheng, J.; Bao, J.; Xuan, N.; Sun, Y.; Liu, B.; Xie, A.; Wu, S.; Sun, Z. Chemical and Bandgap Engineering in Monolayer Hexagonal Boron Nitride. *Sci. Rep.* **2017**, *7* (1), 45584.

(7) Korona, T.; Chojecki, M. Exploring Point Defects in Hexagonal Boron-Nitrogen Monolayers. *Int. J. Quantum Chem.* **2019**, *119* (14), No. e25925.

(8) Raza, A.; Qumar, U.; Hassan, J.; Ikram, M.; Ul-Hamid, A.; Haider, J.; Imran, M.; Ali, S. A Comparative Study of Dirac 2D Materials, TMDCs and 2D Insulators with Regard to Their Structures and Photocatalytic/Sonophotocatalytic Behavior. *Appl. Nanosci.* **2020**, *10*, 3875−3899.

(9) Wickramaratne, D.; Weston, L.; Van de Walle, C. G. Monolayer to Bulk Properties of Hexagonal Boron Nitride. *J. Phys. Chem. C* **2018**, *122*, 25524−25529.

(10) BenMoussa, B.; D'Haen, J.; Borschel, C.; Barjon, J.; Soltani, A.; Mortet, V.; Ronning, C.; D'Olieslaeger, M.; Boyen, H. G.; Haenen, K. Hexagonal Boron Nitride Nanowalls: Physical Vapour Deposition, 2D/3D Morphology and Spectroscopic Analysis. *J. Phys. D: Appl. Phys.* **2012**, *45*, 135302.

(11) Hoang, D.-Q.; Pobedinskas, P.; Nicley, S. S.; Turner, S.; Janssens, S. D.; Van Bael, M. K.; Haen, J. D.; Haenen, K. Elucidation of the Growth Mechanism of Sputtered 2D Hexagonal Boron Nitride Nanowalls. *Cryst. Growth Des.* **2016**, *16* (7), 3699−3708.

(12) Sankaran, K. J.; Hoang, D. Q.; Srinivasu, K.; Korneychuck, S.; Turner, S.; Drijkoningen, S.; Pobedinskas, P.; Verbeeck, J.; Leou, K. C.; Lin, I. N.; et al. Engineering the Interface Characteristics on the Enhancement of Field Electron Emission Properties of Vertically Aligned Hexagonal Boron Nitride Nanowalls. *Phys. Status Solidi.* **2016**, *213*, 2654−2661.

(13) Sankaran, K. J.; Hoang, D. Q.; Kunuku, S.; Korneychuk, S.; Turner, S.; Pobedinskas, P.; Drijkoningen, S.; Van Bael, M. K.; D'Haen, J.; Verbeeck, J.; Leou, K.-C.; Lin, I.-N.; Haenen, K. Enhanced Optoelectronic Performances of Vertically Aligned Hexagonal Boron Nitride Nanowalls-Nanocrystalline Diamond Heterostructures OPEN. *Sci. Rep.* **2016**, *6*, 1−11.

(14) Thomas, J. J.; Weston, N. E.; O'Connor, T. E. Turbostratic Boron Nitride, Thermal Transformation to Ordered-Layer-Lattice Boron Nitride. *J. Am. Chem. Soc.* **1962**, *84*, 4619−4622.

(15) Jimenez, M. J. M.; Antunes, V.; Cucatti, S.; Riul, A.; Zagonel, L. F.; Figueroa, C. A.; Wisnivesky, D.; Alvarez, F. Physical and Micro-

Nano-Structure Properties of Chromium Nitride Coating Deposited by RF Sputtering Using Dynamic Glancing Angle Deposition. *Surf. Coat. Technol.* **2019**, *372* (March), 268−277.

(16) Jimenez, M. J. M.; Leidens, L. M.; Boeira, C. D.; Antunes, V. G.; Cemin, F.; Riul, A.; Zagonel, L. F.; Figueroa, C. A.; Wisnivesky, D.; Zanatta, A. R.; et al. Experimental and Theoretical Insights on the Influence of Substrate Oscillation Period on Advanced Coatings Deposited by Dynamic Glancing Angle Deposition. *J. Mater. Res.* **2024**, *40*, 278−291.

(17) Levendorf, M. P.; Kim, C.-J.; Brown, L.; Huang, P. Y.; Havener, R. W.; Muller, D. A.; Park, J. Graphene and Boron Nitride Lateral Heterostructures for Atomically Thin Circuitry. *Nature* **2012**, *488*, 627−632.

(18) Li, W.; Wang, F.; Chu, X. S.; Liu, X. Y.; Dang, Y. Y. Regulation of Bandgap and Interfacial Conductivity: Construction of Carbon-Doped Three-Dimensional Porous h-BN/RGO Hybrid for Hydrogen Evolution. *Appl. Surf. Sci.* **2021**, *560*, 150053.

(19) Merenkov, I. S.; Burovihina, A. A.; Zhukov, Y. M.; Kasatkin, I. A.; Medvedev, O. S.; Zvereva, I. A.; Kosinova, M. L. Thermal Stability of UV Light Emitting Boron Nitride Nanowalls. *Mater. Des.* **2017**, *117*, 239−247.

(20) Merenkov, I. S.; Myshenkov, M. S.; Zhukov, Y. M.; Sato, Y.; Frolova, T. S.; Danilov, D. V.; Kasatkin, I. A.; Medvedev, O. S.; Pushkarev, R. V.; Sinitsyna, O. I.; Terauchi, M.; Zvereva, I. A.; Kosinova, M. L.; Ostrikov, K. O.-C. Low-Temperature Plasma Growth and Applications of h-BN Nanosheets. *Nano Res.* **2019**, *12* (1), 91−99.

(21) Hammer, P.; Victoria, N. M.; Alvarez, F. Electronic Structure of Hydrogenated Carbon Nitride Films. *J. Vac. Sci. Technol. A Vacuum, Surfaces, Film.* **1998**, *16* (5), 2941−2949.

(22) Shirley, D. A. High-Resolution x-Ray Photoemission Spectrum of the Valence Bands of Gold. *Phys. Rev. B* **1972**, *5*, 4709−4714.

(23) Wagner, C. D.; Davis, L. E.; Zeller, M. V.; Taylor, J. A.; Raymond, R. H.; Gale, L. H. Empirical Atomic Sensitivity Factors for Quantitative Analysis by Electron Spectroscopy for Chemical Analysis. *Surf. Interface Anal.* **1981**, *3* (5), 211−225.

(24) de Keijser, T. H.; Langford, J. I.; Mittemeijer, E. J.; Vogels, A. B. P. Use of the Voigt Function in a Single-Line Method for the Analysis of X-Ray Diffraction Line Broadening. *J. Appl. Crystallogr.* **1982**, *15* (3), 308−314.

(25) Alvarez, F.; Williams, F. Photoluminescence of Hydrogenated Amorphous Silicon. *J. non-Cryst. Solids.* **1982**, *50* (2), 139−148.

(26) Jimenez, M. J. M.; Antunes, V. G.; Zagonel, L. F.; Figueroa, C. A.; Wisnivesky, D.; Alvarez, F. Effect of the Period of the Substrate Oscillation in the Dynamic Glancing Angle Deposition Technique: A Columnar Periodic Nanostructure Formation. *Surf. Coat. Technol.* **2020**, *383*, 125237.

(27) Moulder, J. F.; Stickle, W. F.; Sobol, P. E.; Bomben, K. D. *Handbook Of x-Ray Photoelectron Spectroscopy; Physical Electronics Division*. Perkin-Elmer Corp., Eden Prairie: United States of America, 1992.

(28) Deng, J.; Chen, G. Surface Properties of Cubic Boron Nitride Thin Films. *Appl. Surf. Sci.* **2006**, *252* (22), 7766−7770.

(29) Guimon, C.; Gonbeau, D.; Pfister-Guillouzo, G.; Dugne, O.; Guette, A.; Naslain, R.; Lahaye, M. XPS Study of BN Thin Films Deposited by CVD on Sic Plane Substrates. *Surfaces Interfaces Anal.* **1990**, *16*, 440−445.

(30) Hou, L.; Chen, Z.; Liu, X.; Gao, Y.; Jia, G. X-Ray Photoelectron Spectroscopy Study of Cubic Boron Nitride Single Crystals Grown under High Pressure and High Temperature. *Appl. Surf. Sci.* **2012**, *258* (8), 3800−3804.

(31) Schild, D.; Ulrich, S.; Ye, J.; Stüber, M. XPS Investigations of Thick, Oxygen-Containing Cubic Boron Nitride Coatings. *Solid State Sci.* **2010**, *12* (11), 1903−1906.

(32) Moussa, G.; Salameh, C.; Bruma, A.; Malo, S.; Demirci, U. B.; Bernard, S.; Miele, P. Nanostructured Boron Nitride: From Molecular Design to Hydrogen Storage Application. *Inorganics* **2014**, *2*, 396−409.

(33) Kumar, A.; Malik, G.; Sharma, S.; Chandra, R.; Mulik, R. S. Precursors Controlled Morphologies of Nanocrystalline H-BN and Its Growth Mechanism. *Ceram. Int.* **2021**, *47* (21), 30985−30992.

(34) Aradi, E.; Naidoo, S. R.; Billing, D. G.; Wamwangi, D.; Motochi, I.; Derry, T. E. Ion Beam Modification of the Structure and Properties of Hexagonal Boron Nitride: An Infrared and X-Ray Diffraction Study. *Nucl. Instruments Methods Phys. Res. Sect. B Beam Interact. With Mater. Atoms* **2014**, *331*, 140−143.

(35) Coudurier, N.; Chubarov, M.; Boichot, R.; Mercier, F.; Blanquet, E.; Reboud, R.; Lay, S.; Crisci, A.; Coindeau, S.; Encinas, T.; Pons, M. Growth of Boron Nitride Films on W-AlN (0001), 4° off-Cut 4H-SiC (0001), W (110) and Cr (110) Substrates by Chemical Vapor Deposition. *Cryst. Res. Technol.* **2016**, *51*, 231−238.

(36) Alkoy, S.; Toy, C.; Gönül, T.; Tekin, A. Crystallization Behavior and Characterization of Turbostratic Boron Nitride. *J. Eur. Ceram. Soc.* **1997**, *17* (12), 1415−1422.

(37) Chen, Y.; Liang, H.; Abbas, Q.; Liu, J.; Shi, J.; Xia, X.; Zhang, H.; Du, G. Growth and Characterization of Porous Sp2-BN Films with Hollow Spheres under Hydrogen Etching Effect via Borazane Thermal CVD. *Appl. Surf. Sci.* **2018**, *452*, 314−321.

(38) Dekempeneer, E. H. A.; Kuypers, S.; Vercammen, K.; Meneve, J.; Smeets, J.; Gibson, P. N.; Gissler, W. Scratch-Resistant Transparent Boron Nitride Films. *Surf. Coat. Technol.* **1998**, *100−101* (1−3), 45−48.

(39) Cemin, F.; de Mello, S. R. S.; Figueroa, C. A.; Alvarez, F. Influence of Substrate Bias and Temperature on the Crystallization of Metallic NbTaTiVZr High-Entropy Alloy Thin Films. *Surf. Coat. Technol.* **2021**, *421*, 127357.

(40) Nemanich, R. J.; Solin, S. A.; Martin, R. M. Light Scattering Study of Boron Nitride Microcrystals. *Phys. Rev. B* **1981**, *23*, 6348−6356.

(41) Yu, J.; Qin, L.; Hao, Y.; Kuang, S.; Bai, X.; Chong, Y. M.; Zhang, W.; Wang, E. Vertically Aligned Boron Nitride Nanosheets: Chemical Vapor Synthesis, Ultraviolet Light Emission, and Superhydrophobicity. *ACS Nano* **2010**, *4*, 414−422.

(42) Geick, R.; Perry, C. H.; Rupprecht, G. Normal Modes in Hexagonal Boron Nitride. *Phys. Rev.* **1966**, *146*, 543−547.

(43) Kabbara, H.; Kasri, S.; Brinza, O.; Bauville, G.; Gazeli, K.; Sousa, J. S.; Mille, V.; Tallaire, A.; Lombardi, G.; Lazzaroni, C. A Microplasma Process for Hexagonal Boron Nitride Thin Film Synthesis. *Appl. Phys. Lett.* **2020**, *116* (17), 171902.

(44) Yamada, H.; Inotsume, S.; Kumagai, N.; Yamada, T.; Shimizu, M. Growth Temperature Effects of Chemical Vapor Deposition-Grown Boron Nitride Layer Using B 2 H 6 and NH 3. *Phys. Status Solidi.* **2020**, *257* (4), 1900521.

(45) Ahmad, P.; Khandaker, M.U.; Rehman, F.; Muhammad, N.; Faruque, M.R.I.; Ullah, Z.; Khan, M.A.R.; Khan, G.; Khan, M.I.; Ali, H.; et al. Facile Synthesis of High-Quality Nano-Size 10 B-Enriched Fibers of Hexagonal Boron Nitride. *Crystal* **2021**, *11*, 222.

(46) Sudeep, P. M.; Vinod, S.; Ozden, S.; Sruthi, R.; Kukovecz, A.; Konya, Z.; Vajtai, R.; Anantharaman, M. R.; Ajayan, P. M.; Narayanan, T. N. Functionalized Boron Nitride Porous Solids. *RSC Adv.* **2015**, *5*, 93964−93968.

(47) Werninghaus, T.; Friedrich, M.; Hahn, J.; Richter, F.; Zahn, D. R. T. Raman Spectroscopy Investigation of Cubic Boron Nitride Single Crystals and Layers on Si(100). *Diamond Relat. Mater.* **1997**, *6* (5−7), 612−616.

(48) Shishonok, E. M.; Steeds, J. W. On the Curve of the Density of Phonon States for Cubic Boron Nitride (from the Results of Photoluminescence Measurements). *Phys. Solid State.* **2007**, *49* (9), 1744−1748.

(49) Sutter, P.; Lahiri, J.; Zahl, P.; Wang, B.; Sutter, E. Scalable Synthesis of Uniform Few-Layer Hexagonal Boron Nitride Dielectric Films. *Nano Lett.* **2013**, *13*, 276−281.

(50) Zanatta, A. R. Revisiting the Optical Bandgap of Semiconductors and the Proposal of a Unified Methodology to Its Determination. *Sci. Rep.* **2019**, *9* (1), 11225.

(51) Feng, S.; Lin, Z.; Gan, X.; Lv, R.; Terrones, M. Doping Two-Dimensional Materials: Ultra-Sensitive Sensors, Band Gap Tuning and Ferromagnetic Monolayers. *Nanoscale Horiz.* **2017**, *2* (2), 72−80.

(52) Li, J.; Gui, G.; Zhong, J. Tunable Bandgap Structures of Two-Dimensional Boron Nitride. *J. Appl. Phys.* **2008**, *104* (9), 094311.

(53) Mengle, K. A.; Kioupakis, E. Impact of the Stacking Sequence on the Bandgap and Luminescence Properties of Bulk, Bilayer, and Monolayer Hexagonal Boron Nitride. *APL Mater.* **2019**, *7* (2), 021106.

(54) Weng, Q.; Kvashnin, D. G.; Wang, X.; Cretu, O.; Yang, Y.; Zhou, M.; Zhang, C.; Tang, D. M.; Sorokin, P. B.; Bando, Y.; et al. Tuning of the Optical, Electronic, and Magnetic Properties of Boron Nitride Nanosheets with Oxygen Doping and Functionalization. *Adv. Mater.* **2017**, *29* (28), 1700695.

(55) Pankove, J. I.; Noble, M. J.*Hydrogen In Semiconductors: Semiconductor And Semimetals*Academic Press: San Diego, 1991, Vol. *34*, PP1-15. DOI: .

(56) Peng, Q. Strain-Induced Dimensional Phase Change of Graphene-like Boron Nitride Monolayers. *Nanotechnology* **2018**, *29* (40), 405201.

(57) Ohlsson, T. Cutting with Occam's Razor. *Phys. Rev. D* **2012**, *86* (9), 097301.

(58) Wang, Q.; Zhang, Q.; Zhao, X.; Luo, X.; Wong, C. P. Y.; Wang, J.; Wan, D.; Venkatesan, T.; Pennycook, S. J.; Loh, K. P.; Eda, G.; Wee, A. T. S. Photoluminescence Upconversion by Defects in Hexagonal Boron Nitride. *Nano Lett.* **2018**, *18* (11), 6898−6905.

(59) Wang, B. B.; Zhu, M. K.; Ostrikov, K.; Levchenko, I.; Keidar, M.; Shao, R. W.; Zheng, K.; Gao, D. Conversion of Vertically-Aligned Boron Nitride Nanowalls to Photoluminescent CN Compound Nanorods: Efficient Composition and Morphology Control via Plasma Technique. *Carbon* **2016**, *109*, 352−362.

(60) Jin, M.-S.; Kim, N.-O. Photoluminescence of Hexagonal Boron Nitride (h-BN) Film. *J. Electr. Eng. Technol.* **2010**, *5* (4), 637−639.

(61) Prakash, A.; Sundaram, K. B.; Campiglia, A. D. Photoluminescence Studies on BCN Thin Films Synthesized by RF Magnetron Sputtering. *Mater. Lett.* **2016**, *183*, 355−358.

(62) Li, H.; Zhu, S.; Zhang, M.; Wu, P.; Pang, J.; Zhu, W.; Jiang, W.; Li, H. Tuning the Chemical Hardness of Boron Nitride Nanosheets by Doping Carbon for Enhanced Adsorption Capacity. *ACS Omega* **2017**, *2* (9), 5385−5394.

(63) Raidongia, K.; Nag, A.; Hembram, K. P. S. S.; Waghmare, U. V.; Datta, R.; Rao, C. N. R. BCN: A Graphene Analogue with Remarkable Adsorptive Properties. *Chem. - A Eur. J.* **2010**, *16* (1), 149−157.

(64) Vokhmintsev, A.; Weinstein, I.; Zamyatin, D. Electron-Phonon Interactions in Subband Excited Photoluminescence of Hexagonal Boron Nitride. *J. Lumin.* **2019**, *208*, 363−370.

(65) Yan, S. Negative Thermal Quenching of Photoluminescence: An Evaluation from the Macroscopic Viewpoint. *Materials* **2024**, *17* (3), 586.

(66) Okashiro, Y.; Takashima, H.; Shimazaki, K.; Suzuki, K.; Mukai, Y.; Aharonovich, I.; Takeuchi, S. Selective Anti-Stokes Excitation of a Single Defect Center in Hexagonal Boron Nitride. *ACS Photonics* **2024**, *11* (9), 3602−3609.

(67) Wang, X.; Zhao, D.; Ning, J.; Yu, D.; Xu, S. Large Negative Thermal Quenching and Broadening Lineshape Analysis of Acceptor-Associated Yellow Luminescence in Si-Doped GaN. *J. Phys. Chem. C* **2022**, *126* (48), 20686−20693.

(68) Ley, L.Joannopoulos, J. D.; Lucovsky, G.The Physics of Hydrogenated Amorphous Silicon II Topics in Applied Physics; Springer: Berlin Heidelberg: Berlin, Heidelberg. 1984, Vol:55. DOI:

(69) Mendelson, N.; Chugh, D.; Reimers, J. R.; Cheng, T. S.; Gottscholl, A.; Long, H.; Mellor, C. J.; Zettl, A.; Dyakonov, V.; Beton, P. H.; Novikov, S. V.; Jagadish, C.; Tan, H. H.; Ford, M. J.; Toth, M.; Bradac, C.; Aharonovich, I. Identifying Carbon as the Source of Visible Single-Photon Emission from Hexagonal Boron Nitride. *Nat. Mater.* **2021**, *20* (3), 321−328.

(70) Zhong, D.; Gao, S.; Saccone, M.; Greer, J. R.; Bernardi, M.; Nadj-Perge, S.; Faraon, A. Carbon-Related Quantum Emitter in Hexagonal Boron Nitride with Homogeneous Energy and 3-Fold Polarization. *Nano Lett.* **2024**, *24* (4), 1106−1113.